ORIGINAL ARTICLE

Antibacterial and anticancer activity of ZnO with different morphologies: a comparative study

S. C. Esparza González[1] · Ena Bolaina-Lorenzo[3] · J. J. Pérez-Trujillo[2] · B. A. Puente-Urbina[3] · O. Rodríguez-Fernández[3] · A. Fonseca-García[4] · R. Betancourt-Galindo[3]

Abstract

ZnO nanoparticles (NPS) with different morphologies were synthesized, and the antibacterial and anticancer activity was studied, herein. The physicochemical characterization was carried out by X-ray diffraction (XRD), transmission electron microscopy (TEM), Fourier-transform infrared spectroscopy (FTIR) and UV–visible. To study the antibacterial and anticancer capability of ZnO NPS, *Escherichia coli (E. coli)* and *Staphylococcus aureus (S. aureus)* bacteria and HeLa cancer cells were exposed at different doses of ZnO NPS (7–250 µg/mL). TEM analysis confirmed the obtention of spherical, hexagonal and rod ZnO NPS with an average diameter of 20 ± 4 nm, 1.17 ± 0.3 µm and 1.11 ± 1.2 µm, respectively. XRD diffractograms showed the characteristic pattern of crystalline ZnO in wurtzite phase. FTIR and UV–vis spectra showed slight differences of the main absorption peaks, revealing that different ZnO NPS morphologies may cause shifts in spectra. Biological essays showed that the number of *E. coli* and *S. aureus* bacteria as well as HeLa cells decreases linearly by increasing the nanoparticle concentration. However, the best anticancer and antibacterial activity was shown by spherical ZnO NPS at 100 µg/mL. The better capability of spherical ZnO NPS than hexagonal and rod ZnO NPS is related with its small particle size. The present results suggest that the spherical ZnO NPS has a great potential as an antibacterial and anticancer agent.

Introduction

Metallic materials such as gold, silver, copper, copper oxide, titanium dioxide (TiO_2) and zinc oxide (ZnO) have demonstrated great potential in antibacterial and anticancer applications (Sivakumar et al. 2018). Particularly, ZnO has gained great interest in the scientific community due to its anticancer and antibacterial capabilities, as well as for its affordability and availability in nature. The antibacterial capability of ZnO has been tested against several Gram-positive and Gram-negative bacteria like *Escherichia coli* (*E. coli*), *Staphylococcus aureus* (*S. aureus*), *Pseudomonas aeruginosa, and Bacillus subtilis* (Chakra et al. 2017; Hussain et al. 2019), to name a few. One of the ZnO nanoparticle mechanisms to inhibit bacteria is related to its ability to disintegrate the cell membrane (Jacob et al. 2019a, b) through oxidative stresses which in turn is induced by the formation of reactive oxygen species (ROS) (Shabaani et al. 2020). On the other hand, reports focused on the potential application of ZnO as anticancer agent agree that also ROS along with apoptosis and necrosis are the main cell death mechanisms (Sisubalam et al. 2018, Hussain et al. 2019). The anticancer activity is probably related not only to the above-mentioned mechanisms but also to the cell membrane rupture during the particle migration within the cells (Lin et al. 2009). For instance, Fadoju et al. (2019) observed that spherical TiO_2 nanoparticles (NPS) enter more easily than irregular-shaped

✉ R. Betancourt-Galindo
  rebeca.betancourt@ciqa.edu.mx

1   School of Dentistry, Saltillo Campus, Autonomous University of Coahuila, Adolfo Lopez Mateos, 25125 Saltillo, Coahuila, Mexico

2   School of Medicine, Autonomous University of Nuevo Leon, 64460 San Nicolás de los Garza, Nuevo Leon, Mexico

3   Center for Research in Applied Chemistry, Blvd. Enrique Reyna No. 140, Col. San José de Los Cerritos, 25294 Saltillo, Coahuila, Mexico

4   Consejo Nacional de Ciencia y Tecnología (CONACYT)-Centro de Investigación en Química Aplicada (CIQA), Blvd. Enrique Reyna Hermosillo 140, 25294 Saltillo, Coahuila, Mexico

ZnO NPS on liver cells. Moreover, Bhattacharya et al. (2014) studied cellular uptake of rod and spherical ZnO NPS with similar dimensions, finding out higher cellular infiltration when rod ZnO NPS were used. These studies suggest that the migration of metallic NPS depends on the particle size and shape. Thus, cell membrane rupture is another mechanism that leads cell viability reduction. Raza et al. (2016) and Hussain et al. (2019) independently explored the dual capability of spherical ZnO NPS against bacteria and cancer cells, and confirmed that ROS formation, apoptosis, necrosis and cell membrane rupture are the dominant mechanisms of cell death. Although the dual capability of ZnO NPS for anticancer and antibacterial applications has been proved, the role of the morphological properties (e. g., sized and shape) has not been assessed. Therefore, in this work, ZnO NPS with three different morphologies (viz. spherical, hexagonal and rod-like) were synthesized and tested against *E. coli*, *S. aureus* bacteria and HeLa cancer cells.

Materials and methods

Synthesis of ZnO nanoparticles

Zinc acetate dihydrate ($Zn(CH_3COO)_2 \bullet 2H_2O$, ZnAc, 99%), Triethanolamine (TEA, 99%) and n-propylamine (C_3H_9N, 98%), were purchased from Sigma Aldrich (St. Louis, MO, USA) and used as received. Industrial-grade ethanol (Sumilab, Saltillo, Mexico) and deionized water were purified by distillation for the ZnO synthesis.

ZnO NPS were prepared with different quantities of ZnAc and reaction times to obtain nanoparticles with spherical, hexagonal or rod morphologies. The synthesis was performed mixing two solutions, the first one contained 8.93 or 17.8 g of ZnAc dissolved in a water/TEA (300 mL/5.36 mL) mixture, and the second one was a n-propylamine/ethanol (1.42 mL/1700 mL) mixture. Both solutions were incorporated and stirred at 80 °C for 6 or 12 h depending on the desired structure (Table 1). To recover the formed ZnO NPS, the solution was centrifuged, and the supernatant was discarded. The synthesis product was washed with plenty of ethanol to remove unreacted reagents and dried in a vacuum oven at room temperature for 12 h. This protocol is based on

the method of Hsein et al. (2007) where the n-propylamine played the role of precipitant agent of nanoparticles.

Crystallographic and morphological characterization

The crystalline structure of ZnO NPS was analyzed by X-ray diffraction (XRD) in a Siemens D-5000 diffractometer (CuKα radiation, $\lambda = 1.5418$ Å, SIEMENS, Munich, GER). The crystal size was calculated according to Debye–Scherrer equation. The morphology of the ZnO NPS was observed by high-resolution transmission electron microscopy (HRTEM, Titan 80–300 kV, FEI company, Hillsboro, OR, USA).

Physicochemical characterization

For the identification of molecular structure, Fourier-transform infrared spectroscopy (FTIR) analyses were done. ZnO NPS were mixed in potassium bromide powder and pressed in pellet; the analysis was performed in a Nicolet Magna-IR Spectrometer 550 (Thermo Fisher Scientific Inc., Madison, WI, USA). Raman spectra were recorded using a Horiba Scientific Raman Xplora One spectrophotometer (Clifton Park, NY, USA) coupled to a 785 nm laser. Samples were analyzed for 60 s at 50X and filter position at 10%. The mass loss of ZnO NPS was analyzed using a thermogravimetric analyzer TGA Q500 (TA Instruments, USA). Samples were heated at 10 °C·min^{-1} from 50 to 800 °C under nitrogen atmosphere. Optic properties of ZnO NPS were evaluated with spectrometer UV–Vis NIR Cary 5000 (Agilent Technologies, USA).

Antibacterial activity

Bacterial strains and trypticase soy broth (TSB) were purchased from American Type Culture Collection (ATCC, Manassas, VA, USA). The antibacterial activity of ZnO NPS was tested against gram-negative *E. coli* (ATCC-25922) and gram-positive S. aureus (ATCC-29213) bacteria according to Clinical and Laboratory Standard Institute broth microdilution method (Jorgensen et al. 2015). Bacterial strains were cultured for 24 h at 37 °C in 1:500 TSB, then suspensions of each microorganism were adjusted to approximately 5×10^5 colony forming unit (CFU)/mL. The bacterial suspension was used as inoculum in the antibacterial assays.

For the analysis of the ZnO NPS antibacterial activity, serial dilutions of the nanoparticles were made. The initial concentration of the nanoparticles in TSB (500 µg/mL) was diluted several times to obtain 250, 125, 62.5, 31.2, 15.6 and 7.8 µg/mL. Then, 100 µL of bacterial inoculum was added to two milliliters of each suspension and incubated at 37 °C for 24 h. Culture broth with and without bacteria were used as positive and negative control, respectively.

Table 1 Synthesis parameters to obtain ZnO NPS with spherical, hexagonal or rod morphologies by adding different quantities of zinc acetate dihydrate (ZnAc)

Reaction	ZnAc (g)	Temperature (°C)	Time (h)	Morphology
1	8.928	80	12	Spherical
2	8.928	80	6	Hexagonal
3	17.775	80	6	Rod

Then, the bacterial growth was analyzed by CFU count. All experiments were performed in triplicate and the data were analyzed according to Bonferroni multiple comparison test.

Anticancer activity

Anticancer activity of ZnO NPS was tested with Hela cell line (ATCC CCL-2). For this purpose, a cytotoxicity assay was performed by 3-(4,5-dimethylthiazol-2-yl)-2,5-diphenyltetrazolium bromide assay (MTT, Sigma Aldrich St. Louis, MO, USA). Also, the DNA damage after HeLa cells were exposed to ZnO NPS was studied by a comet assay. Cells were grown in Dulbecco's modified Eagle medium (DMEM) supplemented with 10% of fetal bovine serum (FBS), 1% 4-(2-hydroxyethyl)-1-piperazineethanesulfonic acid buffer (HEPES), 1% non-essential amino acids, 1% penicillin/streptomycin and 1% pyruvate. All cell culture media components were purchased from Gibco-BRL (Grand Island, NY, USA). When 90% of confluency was reached, cells were detached by enzymatic digestion using trypsin for 5 min.

For the cytotoxicity assay of the ZnO NPS, HeLa cells were seeded on 96-well plates at 7500 cells/well and incubated at 37 °C with 5% CO_2 for 24 h to allow cell adhesion. After that, the initial culture medium was replaced by a culture medium containing different concentrations of ZnO NPS (100, 75, 50, 25 and 10 µg/mL) and incubated for 24 or 48 h. Then, the culture medium was removed, and the cells were incubated with MTT solution (10 µL of MTT reagent plus 100 µL of fresh media) for 4 h. Finally, the supernatant was removed and 100 µL of dimethyl sulfoxide (Sigma Aldrich) was added to dissolve formazan crystals. The well plates were read on a microplate photometer (Multiskan FC Thermo Fisher Scientific, Waltham, MA, USA) at 595 nm. The percentage of cell viability was determined in terms of cells' absorbance without ZnO NPS, according to the following equation:

Cell viability (%) = (absorbance of cells with NPS/absorbance without NPS) × 100.

Kruskal–Wallis One-Way Analysis of Variance on Ranks was used to determine the statistical differences among groups. Hydrogen peroxide and culture medium were used as positive and negative control, respectively. To analyze the morphology of HeLa cells before and after the exposition of ZnO NPS, culture cells were observed with an optic microscope (Motic, China).

To study the DNA damage, HeLa cells were seeded on 6-well plates (200 000 cells/well) and incubated at 37 °C and 5% CO_2 for 24 h to allow cell adhesion. Then, the cells were exposed to two concentrations (50 and 100 µg/mL) of each ZnO NPS for 24 h. Following, the culture medium with ZnO NPS was discarded and the remaining cells were washed twice with phosphate buffer saline 1X. Subsequently, the cells from each well were detached with trypsin (Sigma Aldrich) and resuspended in DMEM at a final concentration of 1×10^5 cells/mL. Then, cell suspensions were mixed with agarose (1:1) and an aliquot of 20 µL was placed on slides. The slides were incubated at 4 °C for 15 min in dark and after that the slides were immersed in a lysis buffer at 4 °C for 1 h. The DNA was denatured by incubating the slides in alkaline solution for 30 min at 40 °C in the dark. Then, the slides were placed in a horizontal electrophoresis chamber with alkaline buffer at 35 V for 20 min. After the electrophoresis, the samples were washed three times with cold distilled water and fixed with 70% ethanol. Fifteen minutes after fixation, the DNA was stained with the Vista green DNA dye (Abcam, Shanghai, China). DNA damage was assessed by fluorescence microscopy (Axioscope 5 LED, Carl Zeiss, Germany) with the specific filter for FITC. The images were analyzed with CaspLab software to measure the DNA fragmentation. Four replicates for each concentration were made.

Results and discussion

Morphological analysis of ZnO nanoparticles

The morphology of ZnO NPS was studied by TEM analysis (Fig. 1). Spherical, hexagonal and rod shapes were obtained modifying reaction time and reagents mass. When reaction time was set to 12 h, spherical ZnO NPS were obtained with an average diameter of 20 ± 4 nm. If time was reduced to 6 h, ZnO NPS with hexagonal shape with average diameter of 1.17 ± 0.3 µm were obtained. The rod morphology was obtained maintaining reaction parameters for hexagonal morphology but twofold the ZnAc mass. To characterize rod ZnO NPS, the longest side of rods was measured giving an average length of 1.11 ± 1.2 µm. The formation of ZnO NPS initiate with the decomposition of TEA and ZnAc, following the formation of Zn complex [Zn(TEA)]. Then, the Zn complex reacts with -OH group from alcohol to form a zinc hydroxide intermediate that finally form the ZnO molecule (Wahab et al. 2010, Haque et al. 2013). These reports also point out the importance amine group on the morphology. In the present work, when TEA was supplied in low quantity (regarding ZnAc), rod morphology was obtained. When the proportion was increased, a hexagonal morphology was observed. These outcomes are in good agreement with Haque et al. (2013) who report the aspect ratio of nanoparticles is influenced by TEA amount in the system. Moreover, a comparison of spherical and hexagonal ZnO NPS synthesis conditions (Table 1), revealed that reaction time defined the scale and morphology particle. Hexagonal ZnO NPS were formed when the time was set to 6 h, but nanospheres were formed increasing time to 12 h. This fact
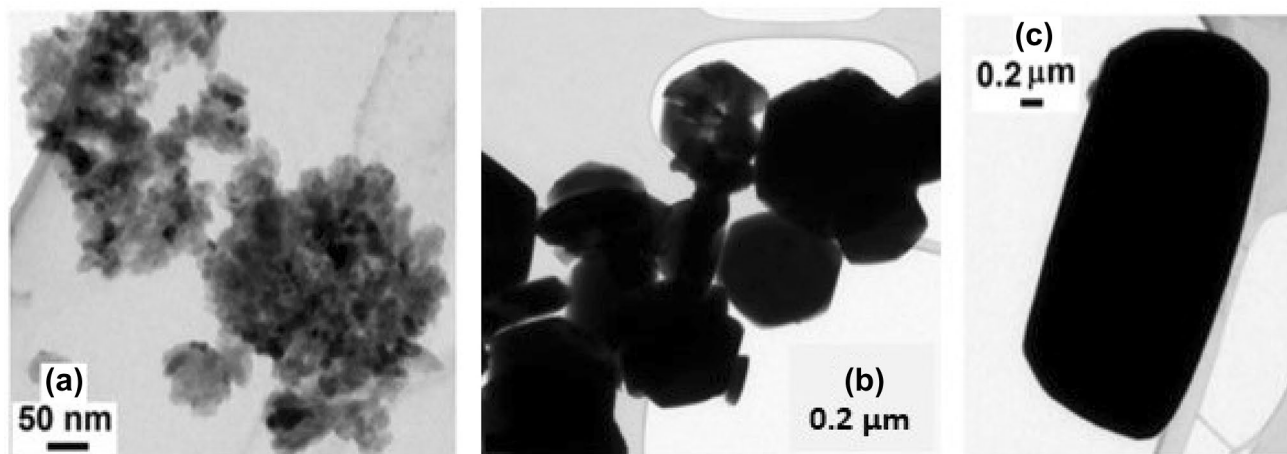
Fig. 1 TEM images of ZnO NPS with (**a**) spherical, (**b**) hexagonal, and (**c**) rod morphologies. The obtained ZnO NPS with spherical, hexagonal and rod morphologies measured an average diameter of 20 ± 4 nm, 1.17 ± 0.3 μm and 1.11 ± 1.2 μm, respectively
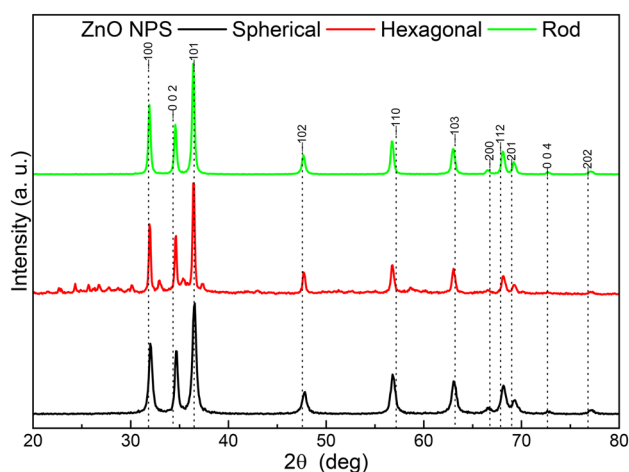
Fig. 2 XRD patterns of ZnO NPS with (**a**) spherical, (**b**) hexagonal, and (**c**) rod morphologies. Diffraction patterns of the three types of ZnO NPS shows the characteristic peaks corresponding to wurtzite structure. These peaks are narrow and well defined suggesting the high crystallinity of ZnO NPS

can be related to the availability of growth units along time that leads to formation of different structures at the early and last stages of the reaction (Hezam et al. 2017).

Crystallographic properties of ZnO nanoparticles

The crystal structure of ZnO NPS was analyzed by X-ray diffraction and the representative patterns are shown in Fig. 2. The diffractograms of all ZnO NPS exhibited diffraction peaks at $2\theta = 31.82°$, $34.33°$, $36.49°$, $47.57°$ $57.17°$ and $63.2°$ which correspond to the (100), (002), (101), (102), (110) and (103) planes of the wurtzite structure (Haque et al. 2013) and is consistent with the data of Joint Committee

on Powder Diffraction standard (JCPDS 74–0534). These peaks are narrow and well defined suggesting the high crystallinity of ZnO NPS (Vinayagam et al. 2019). Furthermore, nanoparticles with high purity were obtained as no other peaks were detected. Crystallite size of the spherical, hexagonal and rod ZnO NPS measured 16, 30 and 26 nm, respectively. Similar crystal sizes have been reported for ZnO NPS obtained by chemical methods (Moharram et al. 2014; Raza et al. 2014).

Physicochemical characterization of ZnO nanoparticles

UV–visible

The UV–Vis absorption spectra of ZnO NPS are presented in Fig. 3. The absorption peaks at 368, 374 and 371 nm for spherical, hexagonal and rod ZnO NPS, respectively, are related to excitonic absorption of ZnO (Chandrasekaran et al. 2012; Brindhadevi et al. 2020). As expected, the spherical ZnO NPS, which has the smallest size, showed the UV–vis peak at lowest wavenumber (Soosen et al. 2009, Haque et al. 2013).

Fourier-transform infrared spectroscopy

FTIR spectra of ZnO NPS with spherical, hexagonal and rod morphology are shown in Fig. 4. The peaks corresponding to Zn–O bond can be observed in the range of 500 to 550 cm^{-1} (Esparza-González et al. 2016; Varadavenkatesan et al. 2019). Interestingly, this peak shifts to higher wavenumbers as the particle sizes increases. In general, the FTIR spectrum can change according to the size
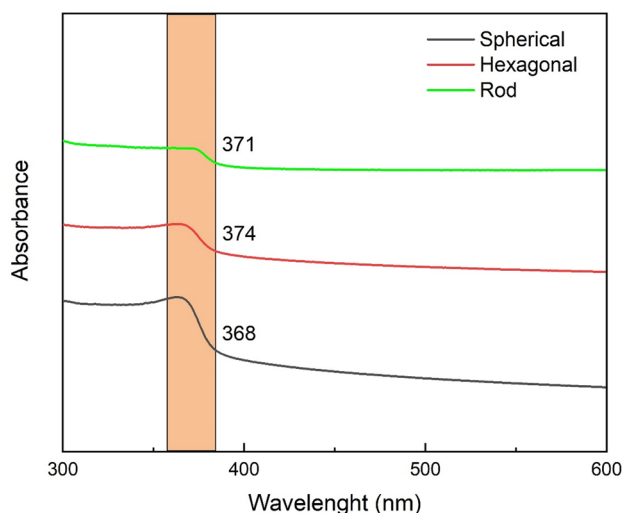
Fig. 3 UV–Vis absorption spectra of ZnO NPS with spherical (black spectrum), hexagonal (red spectrum), and rod (green spectrum) morphologies. The curves showed the main peak at 368, 374 and 371 nm for spherical, hexagonal and rod ZnO NPS, respectively, corresponding to the excitonic absorption of ZnO
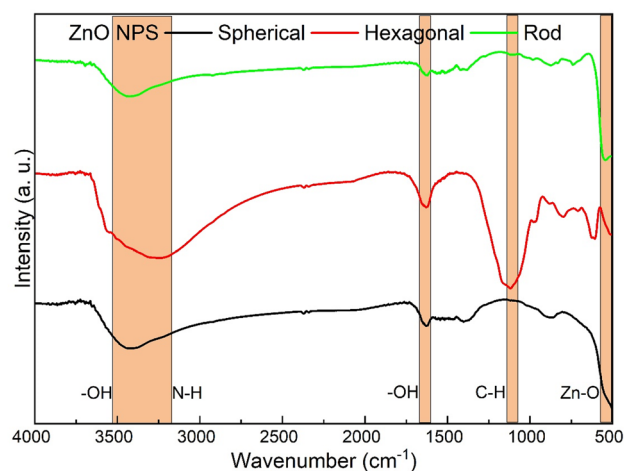
Fig. 4 FTIR spectra of ZnO nanoparticles with spherical (black spectrum), hexagonal (red spectrum), and rod (green spectrum) morphologies. The peak corresponding to Zn–O bond can be observed in the range of 500 to 550 cm^{-1}. This peak shifts to higher wavenumbers as the particle sizes increases

and morphology of NPS (Xie et al. 2011). All ZnO NPS showed peaks around 3400 and 1620 cm^{-1} corresponding to –OH hydroxyl groups (Jacob et al. 2018). Also, the peak around 3400 cm^{-1} is related to vibration of N–H bond and the peak around 1100 cm^{-1} is related to C–H bond from TEA adsorbed on the surface of NPS (Haque and Mahalakshmi 2013; Chandrasekaran et al. 2012). Also, some weak peaks detected in the range of 600–900 cm^{-1}

are related to residual TEA (Talluri et al. 2019). Table 2 list the assignment of detected peaks.

Raman spectroscopy

The Fig. 5 shows representative Raman spectra of spherical, hexagonal and rod ZnO NPS. The wurtzite crystal structure of ZnO belongs to C_6v4 (P63 mc) space group with two formula units per primitive cell where atoms occupy C_3v sites. The group theory indicates ZnO has active phonon modes of A1, E1, 2E2 and a B1 silent mode. Raman spectra of all type of ZnO NPS shows the main characteristic mode E2 at 436 cm^{-1} (Miri et al. 2019; Manikandan et al. 2014). The similarity of all Raman spectra among the samples suggests that regardless of the shape, all ZnO NPS studied in this work has similar chemical structure, which is in good agreement with XRD analyses.

Thermogravimetric analysis

The mass loss and first derivative of ZnO NPS analyzed by TGA are shown in Fig. 6; a similar trend was observed for spherical, hexagonal and rod ZnO NPS. All samples showed a slightly mass loss from 25 to 200 °C which is attributed to the adsorbed water (Mahamuni et al. 2019). A more evident mass loss, associated with OH groups released by dehydroxylation reaction of forming ZnO (Yuvakkumar et al. 2015) was observed between 200 and 450 °C.

Antibacterial activity

The antibacterial activity of spherical, hexagonal and rod ZnO NPS against *E. coli* (Gram negative) and *S. aureus* (Gram positive) was analyzed regarding inhibition of bacterial growth and the results are shown in Fig. 7. According to Bonferroni test, the concentration of 7.8 µg/mL of spherical ZnO NPS did not affect the bacterial growth of either *E. coli* or *S. aureus*, but at higher concentrations (15.6–250 µg/mL), an inhibitory effect is produced in a dose-dependent manner which is comparable with the results reported by Wahab et al. (2010). On the other hand, hexagonal ZnO NPS affected in different ways the growth of *E. coli* and *S. aureus*; the growth of *E. coli* was significantly reduced when the concentration of hexagonal ZnO NPS was ≥ 31.25 µg/mL. In contrast, the best inhibitory effect on the *S. aureus* growth was achieved with 15.6 and 31.5 µg/mL for hexagonal ZnO NPS. As can be seen in Fig. 7, the inhibition of ZnO NPS did not exhibit a linear relationship with the concentration, probably due to nanoparticle agglomeration (Kim et al. 2014). In general, the inhibitory efficiency of hexagonal ZnO NPS on *S. aureus* was much lower regarding *E. coli*. Like previous cases, rod ZnO NPS inhibited the growth of *E. coli* in a dose-dependent manner, but only some doses induced

Table 2 FTIR peak assignment of spherical, hexagonal and rod ZnO NPS

ZnO NPS				
Spherical	Hexagonal	Rod	Peak assignment	References
502	520	545	Zn–O	Esparza-Gonzalez 2016; Varadavenkatesan et al. 2019
Nd	626	Nd	O–H	Talluri et al. 2019
Nd	711	Nd	C–H	Talluri et al. 2019
870	883	875	C–C	Talluri et al. 2019
Nd	1116	1110	C–H	Chandrasekaran
1411	Nd	1421	C–H	Haque
1623	1627	1625	–OH	Rajkumar 2019
3423	3272	3442	–OH, N–H	Rajkumar 2019

Nd not detected
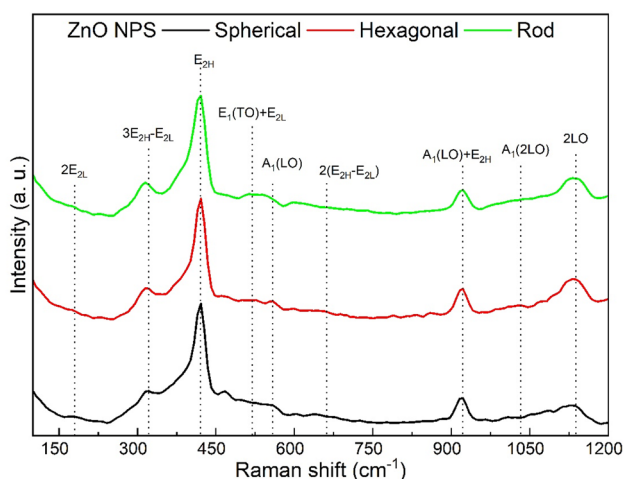
Fig. 5 Raman spectra of ZnO NPS with spherical (black spectrum), hexagonal (red spectrum), and rod (green spectrum) morphologies. The Raman spectra indicates a similar chemical structure for the three types of ZnO NPS

a significant growth inhibition of *S. aureus*. This behavior is related to the fact that the smallest particle size gives a higher antibacterial effect (Mahamuni et al. 2019).

The antibacterial action involves the production and releasing of ROS (like O^-, OH^- and H_2O_2) which depends on the size and active surface area of the particle (Stankovic et al. 2013; Elumalai and Velmurugan 2015). Another possible mechanism is the mechanical damage of bacterial membrane due to the infiltration of nanoparticles inside the cell (Jacob et al. 2019a, b). Based on TEM analysis (Fig. 2), the spherical ZnO NPS exhibited the smallest particle size. These results demonstrate the antibacterial capability of all ZnO NPS against gram-positive and gram-negative bacteria, but the best performance was achieved when spherical ZnO NPS was used. This fact is related to the high releasing of H_2O_2 and small particle size of spherical ZnO NPS.

Anticancer activity

ZnO NPS has great potential as cytotoxic agent for malignant cells. The capability of ZnO NPS to destroy liver (Yuvakkumar et al. 2015) and lung (Lin et al. 2009) carcinoma cells has been previously reported. The anticancer capability of spherical, hexagonal and rod ZnO NPS was analyzed with HeLa cervical cancer cells after 24 (Fig. 8 upper line) and 48 h (Fig. 8 lower line) of culture with ZnO NPS. At 24 h (Fig. 8 upper line), the spherical ZnO NPS produced a decrease of the cell viability in a dose-dependent trend inhibiting most of the cells at 75 μg/mL. According to the ISO 10-993 standard, doses that allow cell viability above 70% are considered non-cytotoxic; this includes the doses of 50, 25 and 10 μg/mL of ZnO NPS in this work. At 48 h (Fig. 8 lower line), the behavior of cell viability of HeLa cells regarding concentration of spherical ZnO NPS was similar to that observed at 24 h but the cytotoxic effect was reached at 50 μg/mL. It is worth to notice that the anticancer capability of the spherical ZnO NPS at 75 μg/mL was similar to that of the positive control for both culture times (*i. e.*, at 24 and 48 h), indicating that the synthesized materials in this work have great anticancer capabilities. On the other hand, some doses of hexagonal and rod (Fig. 8) ZnO NPS caused a negative effect in HeLa cell viability. At 24 and 48 h, the cytotoxic effect was observed at 75 μg/mL and higher concentrations, but cell viability under 50% (Inhibitory Concentration 50, IC_{50}) was achieved only at 100 μg/mL for all cases, in a similar way to the positive control. As a matter of fact, as can be seen in Fig. 9, serious morphological changes in the cell membrane were observed after HeLa cells were exposed to 75 μg/mL of spherical ZnO NPS. In contrast, when hexagonal and rod ZnO NPS was cultured with HeLa cells, the cell damage was more evident when 100 μg/mL was used (Fig. 9). The observed fragmentation and rounded shape are evidence of cell apoptosis and necrosis (Sisubalan et al. 2018). Even though, in general, all ZnO NPS at 100 μg/
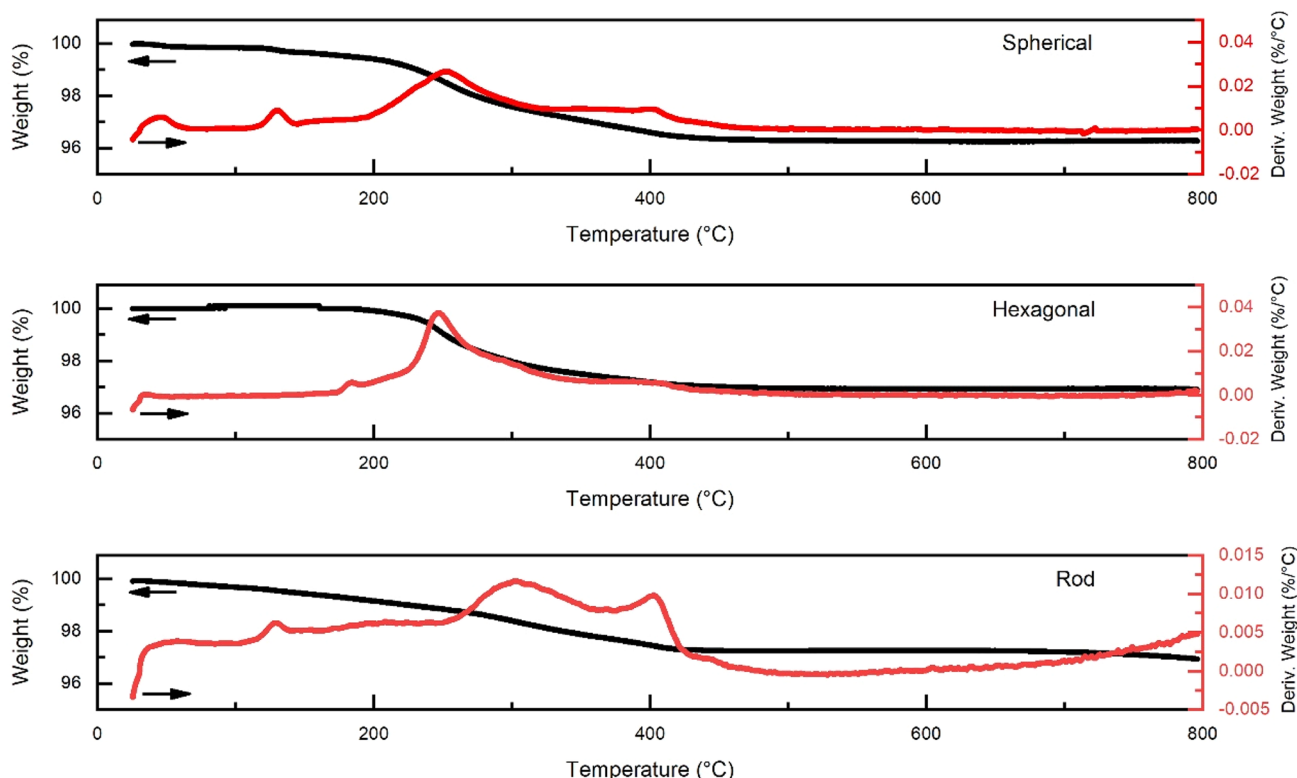
Fig. 6 TG analysis of ZnO NPS with spherical (**a**), hexagonal (**b**), and rod (**c**) morphologies. The mass loss and the first derivative are represented by black and red lines, respectively. All samples showed a slightly mass loss from 25 to 200 °C attributed to the adsorbed water. The mass loss observed between 200 and 450 °C can be associated with OH groups released by the dehydroxylation reaction of forming ZnO

mL of ZnO NPS showed toxicity against cancer cells, the best inhibitory effect was achieved with the smallest particles, which correspond to the spherical shape.

Results of the DNA damage study of HeLa cells at 50 and 100 µg/mL of ZnO NPS are shown in Figs. 10 and 11. The percent of DNA tail, olive moment and tail length (Fig. 10) were higher in HeLa cells treated 100 µg/mL of spherical, hexagonal and rod ZnO NPS compared to HeLa cells without treatment.

In agreement with these findings, comet assay revealed that the dose of 100 µg/mL produced more DNA tail despite the morphology of ZnO NPS.

These outcomes are in good agreement with Hussain et al. (2019) who found an IC_{50} of 100 µg/mL of ZnO NPS for MCF-7, HepG2 and A-549 cancer cells. Sisubalan et al. (2018) reported the reduction of MG-63 cell viability with 10 and 100 µg/mL. Apoptosis and necrosis along with ROS generation by ZnO NPS were the main mechanism for cell death. Additionally, other reports have demonstrated that the anticancer action of ZnO NPS is related to generation of ROS and the contact nanoparticles-cells can cause a malfunction in cellular metabolism (Raza et al. 2016; Paino et al. 2016). The genotoxicity results are in good agreement to that observed by Hackenberg et al. (2011), which observed a linear relationship between the degree of toxicity and nanoparticle concentration. In the light of this results, the higher anticancer capability of spherical ZnO NPS than hexagonal and rod ZnO NPS is related to the smallest particle size.

Conclusions

ZnO nanoparticles with spherical, hexagonal and rod morphologies were studied in terms of antibacterial and anticancer capability. There were quite differences in antibacterial and anticancer behavior of nanoparticles since the interaction between cell and nanoparticle strongly depends on the size. The experiments revealed that the smallest nanoparticles caused high damage to the cell viability of both kinds of cells. As spherical ZnO nanoparticles showed inhibition of cancer and bacteria cells at specific doses, this is a good candidate to be incorporated in medical devices for antibacterial and anticancer therapies.
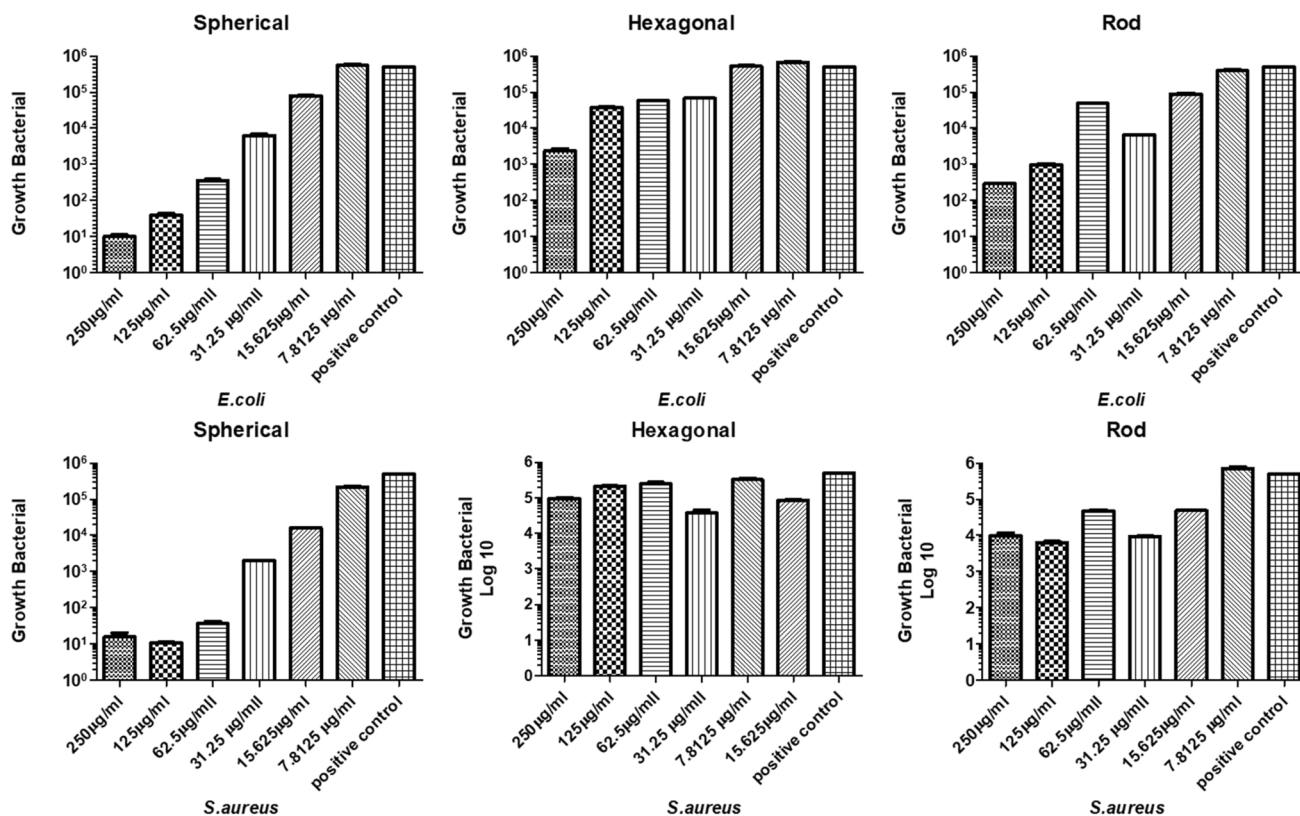
Fig. 7 Bacterial growth of *E. coli* (upper graphs) and *S. aureus* (lower graphs) in presence of ZnO nanoparticles with spherical (**a**), hexagonal (**b**), and rod (**c**) morphologies. Spherical ZnO NPS induced a reduction of bacterial growth in a linear relationship with the concentration; only some doses of hexagonal and rod ZnO NPS reduced the bacterial growth. Culture broth with and without bacteria were used as positive and negative control, respectively. Values are mean $\pm$ SE ($n = 3$) and are statistically significant according to Bonferroni test multiple comparison test ($p \leq 0.05$)
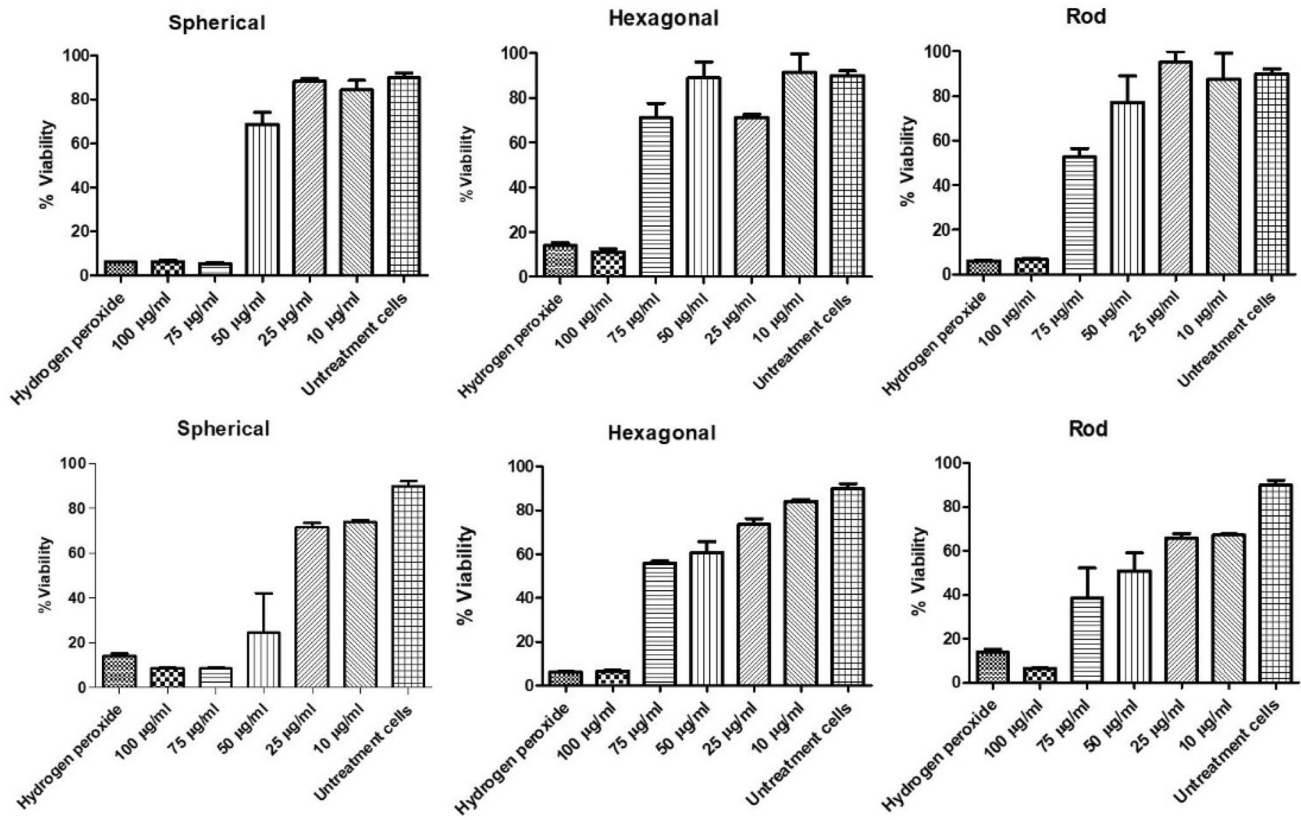
Fig. 8 Cell viability of HeLa cells cultured with ZnO nanoparticles with spherical, hexagonal, and rod morphologies at 24 h (upper graphs) and 48 h (lower graphs). The dose of 100 µg/mL was cytotoxic at 24 and 48 h for all types of ZnO NPS. Values are Mean $\pm$ SE ($n = 3$)
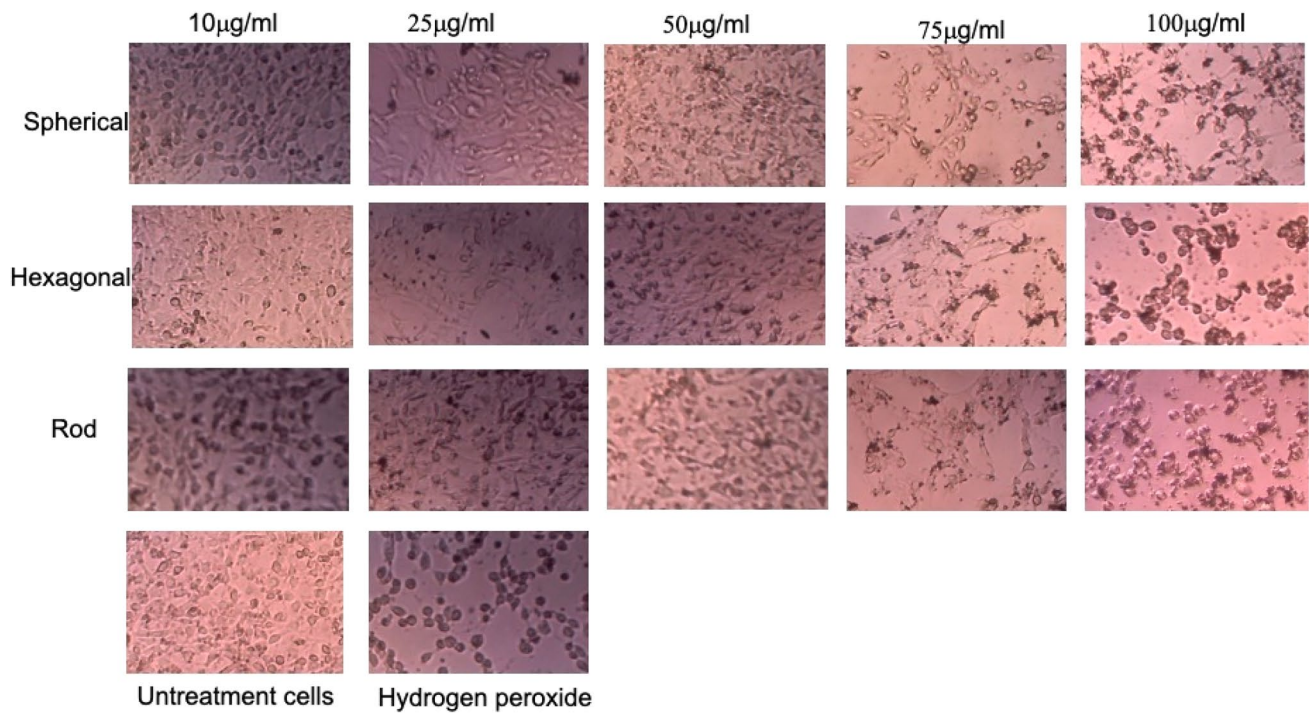
Fig. 9 Images of bright-field microscopy of HeLa cells after 24 h of exposition to spherical, hexagonal and rod ZnO NPS at 10, 25, 50, 75 and 100 μg/mL. At a high ZnO doses, rounded cells are observed, and the number of viable cells is decreased. At low concentrations of ZnO NPS the cell morphology is very similar to the cells without treatment
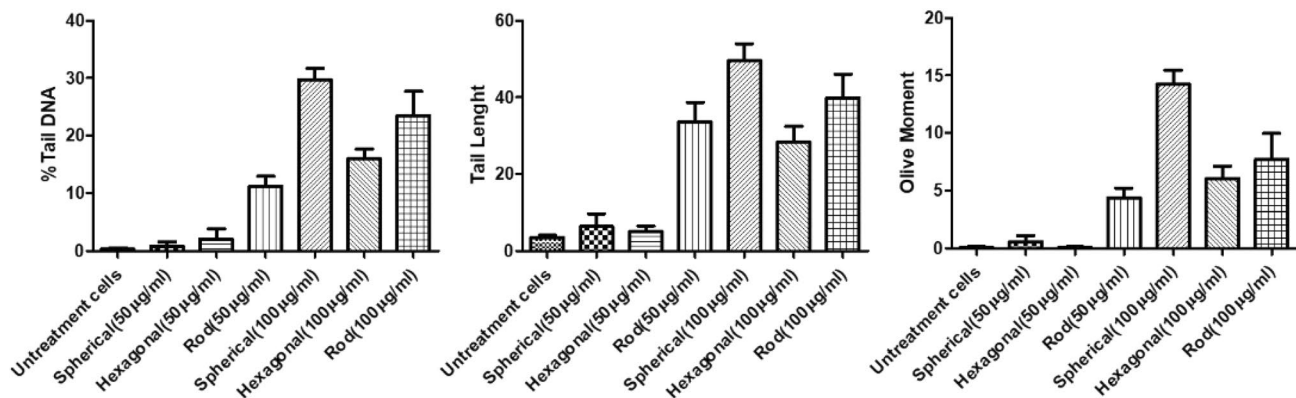
Fig. 10 DNA tail, olive moment, and the tail length of HeLa cells without treatment and treated with 50 and 100 μg/mL of ZnO nanoparticles with spherical, hexagonal, and rod morphologies. Values are Mean $\pm$ SE ($n = 3$). A more extent DNA damage was induced by 100 μg/mL of spherical ZnO NPS
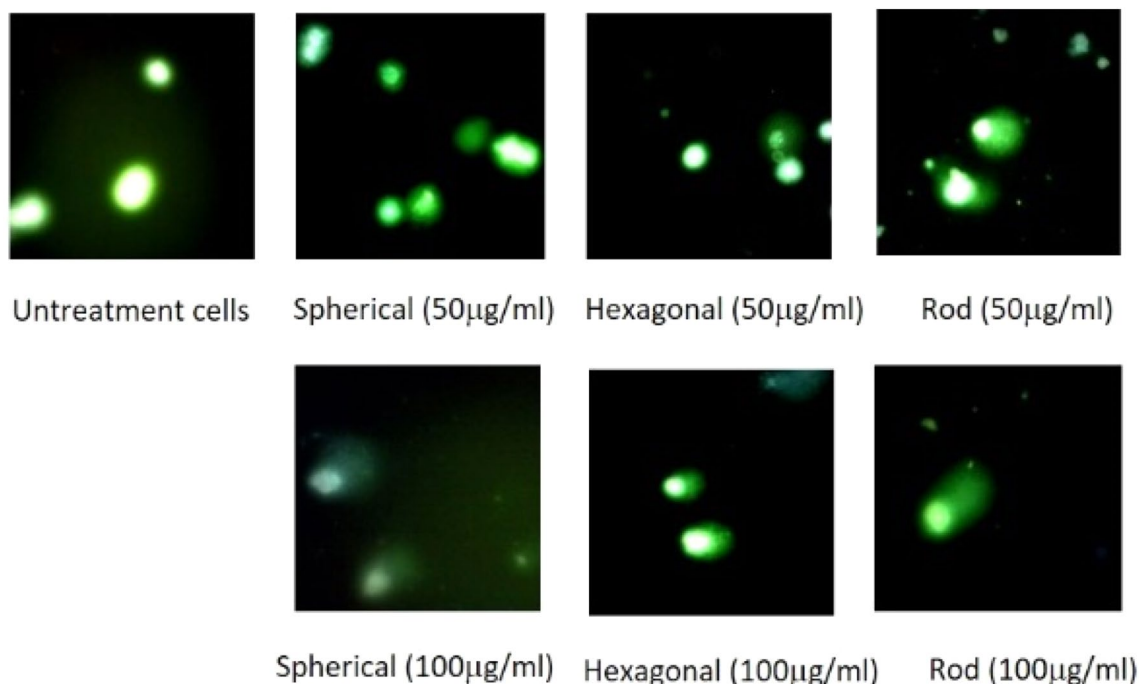
Fig. 11 Fluorescence images of comet assay of HeLa cells treated with spherical, hexagonal and rod ZnO NPS for 24 and 48 h. The HeLa cells treated with 100 µg/mL clearly showed a comet formation indicating DNA damage

Compliance with ethical standards

Conflict of interest The authors declare that they have no conflict of interest in the publication.

References

Bhattacharya D, Santra CR, Ghosh AN, Karmakar P (2014) Differential toxicity of rod and spherical zinc oxide nanoparticles on human peripheral blood mononuclear cells. J Biomed Nanotechnol 10(4):707–716

Brindhadevi K, Samuel MS, Verma TN, Vasantharaj S, Sathiyavimal S, Saravanan M, Pugazhendhi A, Duc PA (2020) Zinc oxide nanoparticles (ZnONPs) -induced antioxidants and photocatalytic degradation activity from hybrid grape pulp extract (HGPE). Biocatal Agric Biotechnol 28:101730

Chakra CHs, Rajendar V, Rao KV, Kumar M (2017) Enhanced antimicrobial and anticancer properties of ZnO and TiO2 nanocomposites. 3 Biotech 7(2): 89

Chandrasekaran P, Viruthagiri G, Srinivasan N (2012) The effect of various capping agents on the surface modifications of sol–gel synthesised ZnO nanoparticles. J Alloys Compd 540(2012):89–93

Elumalai K, Velmurugan S (2015) Green synthesis, characterization and antimicrobial activities of Zinc Oxide nanoparticles from the leaf extract of Azadirachta indica (L.). Appl Surf Sci 345:329–336

Esparza-González SC, Sánchez-Valdés S, Ramírez-Barrón SN, Loera-Arias MJ, Bernal J, Meléndez-Ortiz HI, Betancourt-Galindo R (2016) Effects of different surface modifying agents on the cytotoxic and antimicrobial properties of ZnO nanoparticles. Toxicol in Vitro 37:134–141

Fadoju O, Ogunsuyi O, Akanni O, Alabi O, Alimba C, Adaramoye O, Cambier S, Eswara S, Gutleb AC, Bakare A (2019) Evaluation of cytogenotoxicity and oxidative stress parameters in male Swiss mice co-exposed to titanium dioxide and zinc oxide nanoparticles. Environ Toxicol Pharmacol 70:103204

Hackenberg S, Scherzed A, Technau A, Kessler M, Froelich K, Ginzkey C, Koehler C, Burghartz M, Hagen R, Kleinsasser N (2011) Cytotoxic, genotoxic and pro-inflammatory effects of zinc oxide nanoparticles in human nasal mucosa cells in vitro. Toxicol in vitro 25(3):657–663

Haque MA, Mahalakshmi S (2013) Effect of Triethanolamine on Zinc Oxide Nanoparticles. Mater Focus 2:469–474

Hsieh C-H (2007) Spherical Zinc Oxide Nano Particles from Zinc Acetate in the Precipitation Method. J Chin Chem Soc 2007(54):31–34

Hussain A, Oves M, Alajmi MF, Hussain I, Amir S, Ahmed J, Rehman MT, El-Seedif HR, Ali I (2019) Biogenesis of ZnO nanoparticles using Pandanus odorifer leaf extract: anticancer and antimicrobial activities. RSC Adv 9(27):15357–15369

Jacob JM, Rajan R, Aji M, Kurup GG, Pugazhendhi A (2019a) Bio-inspired ZnS quantum dots as efficient photo catalysts for the degradation of methylene blue in aqueous phase. Ceram Int 45(4):4857–4862

Jacob JM, Rajan R, Tom TC, Kumara VS, Kurup GG, Shanmuganathan R, Pugazhendhi A (2019b) Biogenic design of ZnS quantum dots - Insights into their in-vitro cytotoxicity, photocatalysis and biosensing properties. Ceram Int 45(18A):24193–24201

Jorgensen JH and J. D. Turnidge (2015) Susceptibility test methods: dilution and disk diffusion methods. Manual of Clinical Microbiology, Eleventh Edition, pp. 1253–1273: American Society of Microbiology

Kim KM, Choi MH, Lee JK, Jeong J, Kim YR, Kim MK, Paek SM, Oh JM (2014) Physicochemical properties of surface charge-modified ZnO nanoparticles with different particle sizes. Int J Nanomed 9 Suppl 2(Suppl 2): 41–56

Lin W, Xu Y, Huang C, Ma Y, Shannon KB, Chen D, Huang Y (2009) Toxicity of nano- and micro-sized ZnO particles in human lung epithelial cells. J Nanoparticle Res 11:25–39

Mahamuni PP, Patil PM, Dhanavade MJ, Badiger MV, Shadija PG, Lokhande AC, Bohara RA (2018) Synthesis and characterization of zinc oxide nanoparticles by using polyol chemistry for their antimicrobial and antibiofilm activity. Biochem Biophys Rep 17:71–80

Manikandana E, Kavithac G, Kennedy J (2014) Epitaxial zinc oxide, graphene oxide composite thin-films by laser technique for micro-Raman and enhanced field emission study. Ceram Int 40 (10-A): 16065–16070

Miri A, Mahdinejad N, Ebrahimy O, Khatami M, Sarani M (2019) Zinc oxide nanoparticles: Biosynthesis, characterization, antifungal and cytotoxic activity. Mater Sci Eng C Mater Biol Appl 104:109981

Moharram AH, Mansour SA, Hussein MA, Rashad M (2014) Direct Precipitation and Characterization of ZnO Nanoparticles. J Nanomater 2014:716210

Paino IMM, Goncalves FJ, Souza FL, Zucolotto V (2016) Zinc Oxide Flower-Like Nanostructures That Exhibit Enhanced Toxicology Effects in Cancer Cells. ACS Appl Mater Interfaces 8(48):32699–32705

Raza W, Faisal SM, Owais M, Bahnemanncd D, Muneer M (2016) Facile fabrication of highly efficient modified ZnO photocatalyst with enhanced photocatalytic, antibacterial and anticancer activity. RSC Advances 6(82):78335–78350

Shabaani M, Rahaiee S, Zare M, Jafari SM (2020) Green synthesis of ZnO nanoparticles using loquat seed extract; Biological functions and photocatalytic degradation properties. LWT 134:110133

Sisubalan N, Ramkumar VS, Pugazhendhi A, Karthikeyan C, Indira K, Gopinath K, Hameed ASH, Basha MHG (2018) ROS-mediated cytotoxic activity of ZnO and CeO2 nanoparticles synthesized using the Rubia cordifolia L. leaf extract on MG-63 human osteosarcoma cell lines. Environ Sci Pollut Res Int. 25 (11): 10482–10492

Sivakumar P, Lee M, Kim YS, Shim MS (2018) Photo-triggered antibacterial and anticancer activities of zinc oxide nanoparticles. J Mater Chem B 6(30):4852–4871

Soosen SM, Lekshmi B, George KC (2009) Optical properties of ZnO nanoparticles. SB Academic Review XVI, 57–65.

Stankovic A, Dimitrijevic S, Uskokovic D (2013) Influence of size scale and morphology on antibacterial properties of ZnO powders hydrothemally synthesized using different surface stabilizing agents. Colloids Surf B 102:21–28

Talluri B, Thomas T (2019) Physicochemical properties of chimie douce derived, digestively ripened, ultra-small (r<2 nm) ZnO QDs. Colloids Surf A 575:310–317

Varadavenkatesan T, Lyubchik E, Pai S, Pugazhendhi A, Vinayagam R, Selvaraj R (2019) Photocatalytic degradation of Rhodamine B by zinc oxide nanoparticles synthesized using the leaf extract of Cyanometra ramiflora. J Photoch Photobio B 199:111621

Vinayagam R, Selvaraj R, Arivalagan P, Varadavenkatesan T (2020) Synthesis, characterization and photocatalytic dye degradation capability of Calliandra haematocephala-mediated zinc oxide nanoflowers. J Photochem Photobiol B 203:111760

Wahab R, Mishra A, Yun SI, Kim YS, Shin HS (2010) Antibacterial activity of ZnO nanoparticles prepared via non-hydrolytic solution route. Appl Microbiol Biotechnol 87(5):1917–1925

Xie J, Li Y, Zhao W, Bian L, Wei Y (2011) Simple fabrication and photocatalytic activity of ZnO particles with different morphologies. Powder Technol 207(1–3):140–144

Yuvakkumar R, Suresh J, Saravanakumar B, Joseph Nathanael A, Hong SI, Rajendran V (2015) Rambutan peels promoted biomimetic synthesis of bioinspired zinc oxide nanochains for biomedical applications. Spectrochim Acta Part A 137:250–258